ACS central science

Research Article

http://pubs.acs.org/journal/acscii

Dendrites and Pits: Untangling the Complex Behavior of Lithium Metal Anodes through Operando Video Microscopy

Kevin N. Wood,[†,‡] Eric Kazyak,[†] Alexander F. Chadwick,[‡,§] Kuan-Hung Chen,[†] Ji-Guang Zhang,[‡,∥] Katsuyo Thornton,[‡,§] and Neil P. Dasgupta*[,†,‡]

[†]Department of Mechanical Engineering, University of Michigan, Ann Arbor, Michigan 48109, United States

[‡]Joint Center for Energy Storage Research, University of Michigan, Ann Arbor, Michigan 48109, United States

[§]Department of Materials Science and Engineering, University of Michigan, Ann Arbor, Michigan 48109, United States

[∥]Energy and Environment Directorate, Pacific Northwest National Laboratory, Richland, Washington 99352, United States

Supporting Information

ABSTRACT: Enabling ultra-high energy density rechargeable Li batteries would have widespread impact on society. However the critical challenges of Li metal anodes (most notably cycle life and safety) remain unsolved. This is attributed to the evolution of Li metal morphology during cycling, which leads to dendrite growth and surface pitting. Herein, we present a comprehensive understanding of the voltage variations observed during Li metal cycling, which is directly correlated to morphology evolution through the use of operando video microscopy. A custom-designed visualization cell was developed to enable operando synchronized observation of Li metal electrode morphology and electrochemical behavior during cycling. A mechanistic understanding of the complex behavior of these electrodes is gained through correlation with continuum-scale modeling, which provides insight into the dominant surface kinetics. This work provides a detailed explanation of (1) when dendrite nucleation occurs, (2) how those dendrites evolve as a function of time, (3) when surface pitting occurs during Li electrodissolution, (4) kinetic parameters that dictate overpotential as the electrode morphology evolves, and (5) how this understanding can be applied to evaluate electrode performance in a variety of electrolytes. The results provide detailed insight into the interplay between morphology and the dominant electrochemical processes occurring on the Li electrode surface through an improved understanding of changes in cell voltage, which represents a powerful new platform for analysis.

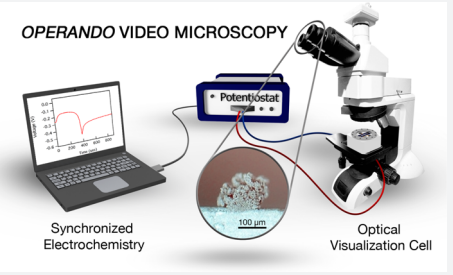

1. INTRODUCTION

As the world's insatiable demand for energy continues to grow, the need for cost-effective and sustainable energy storage devices is paramount. For mobile systems such as electric vehicles (EVs), high energy densities, short recharging times, long cycle-life, and battery safety are essential. Presently, Li ion batteries (LIBs) represent the state of the art in mobile applications. However, the high cost and limited energy density of LIBs have hindered development of 300-mile-per-charge EVs. One of the most attractive strategies to address this challenge is to substitute a Li metal anode for the existing graphite anodes in Li ion batteries. Additionally, stabilization of Li metal is a key step in enabling technologies beyond Li ion, including Li−S and Li−air batteries.[1] The realization of this goal requires an improved understanding of the evolution of Li metal morphology in electrolyte systems relevant to next-generation batteries.

Unfortunately, significant technological hurdles including low Coulombic efficiency (CE), poor cycle life, and safety concerns have prevented widespread Li metal anode commercialization in rechargeable batteries.[2] These challenges can all be linked to the reactivity of Li metal. Undesirable side reactions between the electrolyte and electrode form a solid electrolyte interphase (SEI), consuming active Li[3] and leading to uncontrolled dendrite growth. For decades, researchers have tried to solve this problem, but the mechanism of nucleation and continued propagation of dendrites is still not fully understood. It has been hypothesized that as metallic Li is plated, uneven current distributions resulting from surface inhomogeneities lead to localized "hot spots" where Li preferentially nucleates.[4] On pristine Li substrates this preferential nucleation results in a subsurface disturbance, causing a localized fracture in the SEI. This exposes the underlying bulk Li metal, leading to the formation of a dendrite at that location.[5] The dendrite surface immediately forms an SEI, consuming a significant amount of Li. When polarity is reversed and Li is stripped from the dendrite, the structure can become physically isolated via fracture or mechanical failure. Similarly, Li at the base of the dendrite can be removed, leaving the rest of the structure electronically isolated but still attached to the surface through an insulting SEI layer. Both of these inactive structures are referred to as "dead" Li and will cause reduced CE and result in the removal of Li from the active reservoir.[6,7] While studies

Received: September 1, 2016
Published: October 14, 2016

DOI: 10.1021/acscentsci.6b00260
ACS Cent. Sci. 2016, 2, 790−801

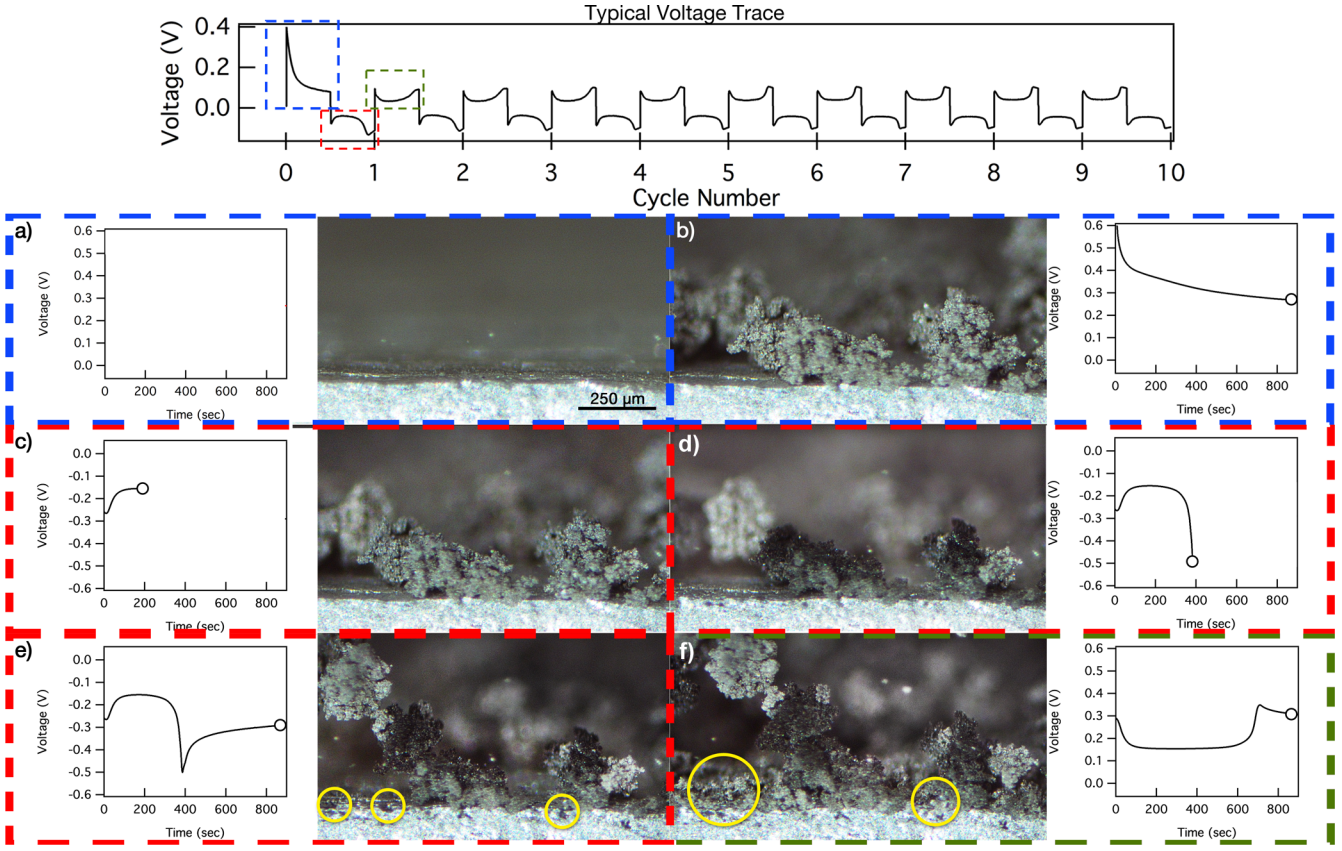

Figure 1. Video 1 still frames for a cell cycled at 5 mA cm^{-2} (two-electrode measurement). EL-b morphology and corresponding voltage trace are shown at times (a) before cycling; (b) after first half-cycle (deposition at EL-b); (c) at cell polarization minimum (dissolution at EL-b); (d) at cell polarization maximum; pitting not yet evident; (e) morphology at end of half-cycle; pitting observed (examples highlighted in yellow circles); (f) morphology at end of third half-cycle (deposition at EL-b); new dendrites are deposited in the pits which formed at the end of the previous half-cycle (yellow circles).

have achieved varying degrees of success in inhibiting dendrite growth,[8−12] there is no consensus on the pathway for mitigation and control of this pernicious effect. This is largely due to the lack of knowledge about the extremely complex interfaces (i.e., those between electrolyte, SEI, native surface layer, and Li metal) where charge transfer occurs in Li metal anodes.[13,14]

The limited understanding of these phenomena is exacerbated by the fact that many studies employ the use of different substrates for Li electrodeposition (Cu, Ni, Pt, etc.). On those substrates Li dendrite nucleation and growth may occur through different mechanisms depending on the substrate properties. This convolutes any interpretation of electrode behavior, as the electrodeposition and electrodissolution of Li on a metallic current collector are not representative of the same processes that occur on bulk Li surfaces. Li−Li symmetric cells provide a more representative platform to describe the behavior of Li metal anodes, since all electrochemical half-reactions occur on a Li surface. This is important because in any secondary battery incorporating a Li metal anode, an excess of Li is required to compensate for imperfect CE.[15] As such, there have been an increasing number of reports comparing Li symmetric cell data.[3,12,16−18] However, a detailed understanding of Li−Li symmetric cells is lacking, due to the complex time-dependent interplay between morphology and electrochemistry occurring at both electrodes.

One of the practical challenges to understanding Li metal behavior stems from the extremely reactive nature of liquid electrolytes and Li metal. This reactivity has also restricted in situ experimental observation in meaningful cell geometries that are representative of battery operation. This limits fundamental knowledge of the process, including the exact location of Li electrodeposition and electrodissolution on electrode surfaces. While a few groups have utilized in situ optical microscopy to observe Li dendrite formation,[19−24] no report has ever linked the time evolving morphological changes observed in the visualization cell with the corresponding changes in electrochemical (voltage) response. This has allowed a level of detail in our mechanistic understanding of reaction pathways and the relationships between morphology and electrochemistry during cycling that has not been previously realized. Recently, in situ transmission electron microscopy (TEM) has provided insight into some aspects of Li dendrite growth at a highly localized scale;[10,13,16,25] however, many questions remain on the effects of dendrites at larger length scales and in cell geometries relevant to practical battery operation.

To this end, we explore in detail the time-dependent voltage response for an applied galvanostatic perturbation in Li−Li symmetric cells, and the resulting changes in electrode morphology. Specifically, the evolution of electrode morphology is observed through operando high-resolution video capture, and is directly correlated to time synchronized voltage traces. A continuum-scale numerical model is developed to relate electrode morphology and competing electrochemical kinetics to cell voltage. This allows for an in-depth understanding of the electrochemical processes occurring on the

DOI: 10.1021/acscentsci.6b00260
ACS Cent. Sci. 2016, 2, 790−801

electrode surfaces, and how the transitions between reaction pathways for electrodeposition and electrodissolution lead to characteristic variations in cell polarization. Based on these results, we demonstrate that galvanostatic voltage traces can be used to infer morphological changes occurring during operation of coin cell battery architectures (where researchers are typically "blind" to morphology evolution). Finally, this interpretation is applied to provide detailed insight into the performance of Li electrodes in electrolytes that exhibit high Coulombic efficiencies. This work provides a level of detailed understanding that will help researchers take the next steps toward making today's "holy grail" of batteries, Li metal anodes, a commercial reality.

2. VISUALIZATION CELL APPROACH AND OBSERVATIONS

2.1. Approach. Evaluation of Li−Li symmetric cells is typically performed by galvanostatic cycling at a fixed current density. This subjects the Li electrode to similar operating conditions to real-world batteries without the need to deconvolute the processes occurring at dissimilar cathode materials. This allows for an evaluation of (1) the cell polarization required to drive electrodeposition and electrodissolution of Li; (2) the cycle life of Li metal electrodes; (3) a quantitative comparison of electrode behavior under varying current densities and electrolytes; and (4) cumulative capacity losses, leading to an evaluation of the average CE.[26] Our recent study on Li−Li symmetric cells also demonstrated that the temporal variations in cell voltage observed during galvanostatic cycling provide an important indication of electrode degradation throughout the cell lifetime. This degradation could be significantly improved through nanoscale surface modifications using atomic layer deposition (ALD).[12,27] Thus, Li−Li symmetric cells represent an important platform to quantitatively evaluate new strategies for stabilization of Li metal, including surface protective layers and new electrolyte chemistries.

Typical data from a two-electrode voltage trace during galvanostatic cycling are shown in Figure 1 (Top). Because this is a Li−Li symmetric cell, time-dependent variations in the cell polarization during cycling are directly representative of overpotentials in the system. In the first half-cycle, an initial decrease in cell voltage is always observed. In subsequent half-cycles, the cell polarization (1) first decreases, (2) reaches a minimum, (3) rises to a local maximum, and (4) decreases again. As a result, a characteristic "peaking" behavior in the voltage trace is observed, as seen in Figure 1. This general form of the voltage trace is consistently observed across a wide range of current densities, electrolyte systems, and cell configurations, while the magnitude and detailed shape of the voltage trace vary based on these parameters. Therefore, an improved understanding of galvanostatic voltage traces provides an important means for evaluating electrode performance.

This general voltage trace behavior has also been observed in a previous study on Li−Li symmetric cells, in which galvanostatic testing and electrochemical impedance spectroscopy (EIS) were used to examine changes in impedance and cell polarization as a function of time.[3] When this electrochemical data was combined with post mortem scanning electron microscopy (SEM), a mechanistic explanation of the overpotential variations was hypothesized based on the observed results. However, ex situ microscopy does not allow for real-time observation of the evolution of dendrite formation and surface pitting, and does not allow for direct correlation of these morphological variations with time-synchronized electrochemical profiles. Moreover, the process of disassembling, drying, and observing a Li metal electrode ex situ does not capture the morphology of the electrode during cell operation, and may lead to significant changes in the surface morphology, affecting the resulting conclusions. To address this challenge, we have developed an operando visualization cell, which allows for direct correlation of real-time high-resolution video capture of the cell morphology during electrochemical cycling to the measured galvanostatic voltage traces (Scheme 1).

Scheme 1. Schematic of Synchronized Electrochemical/Video Microscopy Setup

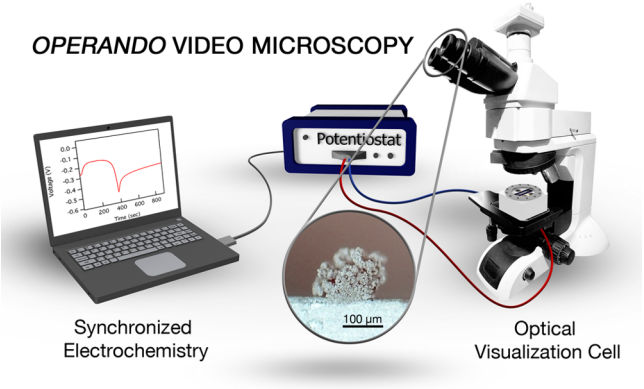

2.2. Experimental Observations. Operando videos of the electrode surface were time-synchronized with the corresponding voltage traces of the cell, as seen in Video 1 and Figure 1. For this initial video, a standard 1 M $LiPF_6$ in 1:1 ethylene carbonate/dimethylcarbonate (EC:DMC) electrolyte was used. The results show the transient morphology of the Li electrode surface for three full cycles in the video, and the first three *half-cycles* of operation in Figure 1 [first cycle charge (Figure 1a,b); first cycle discharge (Figure 1c−e); second cycle charge (Figure 1f)]. In Figure 1b (Video 1 0:00−0:10), dendrites nucleate in unsystematic locations across the surface of the working electrode, shown within the frame (which we will define as ***EL-b***; this definition will not change when polarity is changed). Other dendrites, not in focus, can be observed in the background as well. The corresponding synchronized voltage trace, an inset in the same figure, indicates an initial decrease in cell voltage. As plating continues, the dendrites increase in size, while the morphology and position of the surrounding electrode surface do not change noticeably, implying that the vast majority of Li is plated in dendritic form or contained in the SEI (Figure 1b; Video 1 0:10). Almost immediately upon switching polarity, a maximum cell voltage is observed (Figure 1c; Video 1 0:11). The voltage then quickly *decreases* from the initial maximum as Li continuously transfers to the counter electrode (which we will define as ***EL-a***; this electrode is not in view in Figure 1; this definition will refer to the counter electrode throughout the paper and does not change when polarity is switched), until a minimum in voltage is reached (Figure 1c; Video 1 0:12).

As Li is further stripped from the dendrites, a strong color shift (darkening) is detected on the surface of the stripped dendrites, which correlates with an *increase* in cell voltage (Video 1 0:13). As this reaction proceeds, Li continues to be removed from the previously plated Li (which is exclusively in

DOI: 10.1021/acscentsci.6b00260
ACS Cent. Sci. 2016, 2, 790−801

the form of dendrites on the electrode surface), until all of the electrochemically active Li is removed from the dendritic structures on EL-b (Figure 1d; Video 1 0:14). A local maximum in cell voltage is reached as the source of Li electrodissolution from EL-b is observed to be transitioning from previously plated dendritic Li, to "fresh" bulk Li from the surrounding electrode surface. Here, large portions of the dendrites have changed color to black and are no longer electrochemically active, which we will refer to as "dead" Li (Figure 1d; Video 1 0:14). From this point on in the half-cycle, the color, size, and shape of the dendrites no longer change. As electrodissolution progresses, pits begin to form on the surface of the bulk Li (Figure 1e; Video 1 0:14–0:19), a transition that can be very clearly seen in Video 1. This transition coincides with a second *decrease* in voltage. Pits continue to increase in size, becoming more pronounced. It can also be seen that detached ("dead") Li floats to the surface of the electrolyte in Video 1 at time 0:19.

Upon switching polarity, it can be observed from Figure 1f that new dendrite growth on the surface of EL-b occurs directly within the pits created during the previous half-cycle. This results in a greater number of dendrites on the surface during the second cycle, which are smaller in size than those observed during the first cycle. We note that some of the pitting during the previous half-cycle occurred directly below the locations where "dead" Li is observed. Nucleation of new dendrites in these locations causes the dead Li to be displaced upward. It can also be observed that the exact same shape of the galvanostatic voltage trace is observed for this half-cycle and subsequent half-cycles: two local maxima, a local minimum, and a decrease in cell voltage after pitting begins to occur (Figure 1e,f). This behavior was confirmed to be consistent in the presents of a separator and after several charge/discharge cycles (Video 4; Figure S2). Additionally, control experiments in which the current was periodically interrupted without changing polarity demonstrate that the peaking behavior is not due to a capacitive effect (Figure S3). This general form of initial galvanostatic voltage traces is also observed in Li–Li symmetric coin cell and Swagelok cell geometries (Figure S4). As a result, mechanistic insight into Li metal electrode evolution under operating conditions in typical cell formats and operating pressures can be gained.

3. NUMERICAL MODEL

To provide a theoretical description of the cell behavior, a one-dimensional (1D) numerical continuum-scale model was developed based on previous efforts to study the deposition and dissolution of magnesium metal anodes.[28] The numerical model solves the time-based evolution of the Poisson–Nernst–Planck system of equations (PNP equations) to describe the electrochemical mass transport and the electrostatic potential across the cell. In 1D, the Nernst–Planck equation takes the form

$$J_i = -D_i\frac{\partial c_i}{\partial x} - z_i c_i \frac{D_i F}{RT}\frac{\partial \phi}{\partial x} \tag{1}$$

where J_i is the mass flux of the ith species, D_i is the diffusivity of the species, z_i and c_i are the charge and concentration of the ith species, x is the position, F is Faraday's constant, R is the ideal gas constant, T is the absolute temperature, and ϕ is the electrostatic potential. The 1D Poisson equation takes the form

$$\frac{\partial^2 \phi}{\partial x^2} = -\frac{F}{\epsilon_0 \epsilon_s}\sum_i z_i c_i \tag{2}$$

where ϵ_0 is the vacuum permittivity and ϵ_s is the dielectric constant of the solvent.[29,30] The PNP equations are solved using a backward-implicit finite difference method (FDM) that is similar to those previously developed.[31−35] The model domain is defined as the electrolyte between two parallel planar electrodes. The position of the electrode/electrolyte interface is allowed to change according to the deposition and dissolution flux; therefore, care is taken so that the discretization of the model conserves mass. The reaction at each electrode is governed by Butler–Volmer kinetics, and we employ a modified form of the current–overpotential relationship:

$$i = \gamma F k^0_{\text{eff}}\left[c_{\text{Li}}\exp\left(\frac{(1-\beta)F}{RT}\eta\right) - c_{\text{Li}^+}\exp\left(-\frac{\beta F}{RT}\eta\right)\right] \tag{3}$$

where γ is a parameter that accounts for the roughness of the electrode surface, k^0_{eff} is an effective heterogeneous rate constant that depends upon the morphology of the electrode, β is the symmetry factor, and η is the overpotential of the electrode.[29,30] The roughness parameter, γ, is the ratio between the total surface area of the electrode (including deposits) and the 2D projected surface area.

As observed in the visualization cell, once a dendrite has nucleated, the vast majority of subsequent electrodeposition occurs on the dendrite surface rather than plating onto the surrounding bulk. This suggests that the kinetics of dendrite growth is more rapid than nucleation of new dendrites, which is consistent with time-dependent EIS measurements that were performed immediately after nucleation (Figure S14). Similarly, competing reaction pathways for electrodissolution occur on the opposite electrode. In order to account for different contributing factors to the overall electrode kinetics, the effective heterogeneous rate constant is expanded to include contributions from kinetically fast and slow processes:

$$k^0_{\text{eff}} = \theta_{\text{fast}}k^0_{\text{fast}} + \theta_{\text{slow}}k^0_{\text{slow}} = \theta_{\text{fast}}k^0_{\text{fast}} + (1-\theta_{\text{fast}})k^0_{\text{slow}} \tag{4}$$

where θ_{fast} and θ_{slow} are the fractions of the electrode surface area with fast and slow kinetics, respectively, and k^0_{fast} and k^0_{slow} are the rate constants of the fast and slow processes, respectively. By definition, $\theta_{\text{fast}} + \theta_{\text{slow}} = 1$ because the area fractions must sum to unity. The values of both γ and θ_{fast} depend upon the time-varying surface morphology of the electrode. For the purpose of this simplified model, we approximate the Li deposits during the early stages of nucleation as a uniform square array of hemispheres that grow and eventually impinge during electrodeposition. During electrodissolution, similar assumptions are made, resulting in the deposits contracting and eventually separating (Figure S5). We note that the model does not explicitly account for pitting, but rather considers two processes, one with a larger kinetic constant than the other. More details on the model and its numerical implementation can be found in the Supporting Information.

To complement the experimental data, the model described above was used to simulate the early cycling behavior of the visualization cell during galvanostatic cycling at a current density of 5 mA cm^{-2}. Using the parameters shown in Table S2, the simulated galvanostatic voltage trace shown in Figure 2 is obtained. It can be observed that overall there is very good

DOI: 10.1021/acscentsci.6b00260
ACS Cent. Sci. 2016, 2, 790–801

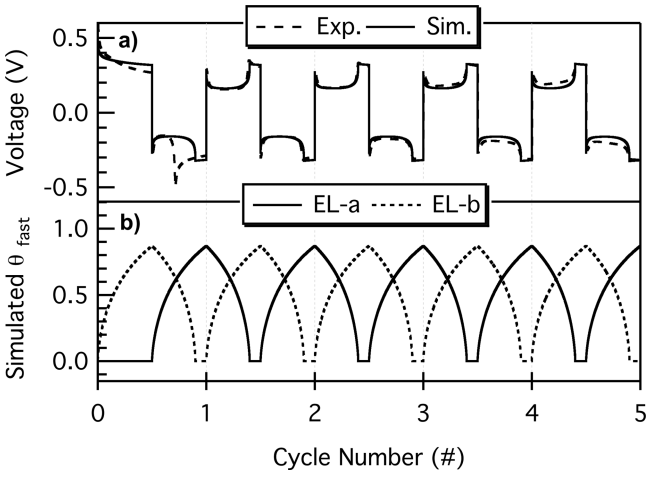

Figure 2. (a) Numerical modeling results of cell polarization showing agreement with experimental data. (b) Simulated area fraction associated with the kinetically fast reaction (θ_{fast}) on each electrode during cycling. When θ_{fast} at the dissolving electrode reaches zero, a maximum in cell voltage occurs.

agreement between the experimental and simulated voltage traces, and both exhibit a characteristic "peaking" voltage profile. In both cases, the cell voltage exhibits a sharp peak at the start of each half-cycle, followed by an asymmetric trough and a subsequent sharp increase leading to a blunted peak before the end of the half-cycle. We note that the model does not fully capture the experimentally observed behavior of the first cycle. This is expected because the model is parametrized for a system that has already been cycled once, which exhibits fundamentally different physical properties than the initial system.

4. RESULTS AND DISCUSSION

Using a combination of numerical modeling and experimental observations, we develop a general framework for interpretation of galvanostatic voltage traces. This framework can be used to provide mechanistic insight into phenomena occurring on Li metal anodes during cycling in a range of relevant battery systems.

4.1. Visualization Cell Interpretation: General Framework. As current is passed through a Li metal electrode, inhomogeneities on the surface lead to an uneven current distribution, resulting in dendrite/pit formation. Contributions to the total current passing through surfaces with different reaction kinetics (such as dendritic and bulk Li) can be expressed in the following form by combining eqs 3 and 4:

$$I_t = iA_{el} = A_{el}\gamma F(\theta_{fast}k^0_{fast} + \theta_{slow}k^0_{slow}) \left[c_{Li}\exp\left(\frac{(1-\beta)F}{RT}\eta\right) - c_{Li^+}\exp\left(-\frac{\beta F}{RT}\eta\right)\right] = g(\eta)(\theta_{fast}k^0_{fast} + \theta_{slow}k^0_{slow}) \quad (5)$$

where $g(\eta)$ consolidates all terms not involving the reaction constants. If we assume that k^0_{fast} and k^0_{slow} are time-invariant, the electrode overpotential will adjust to draw the current required as θ_{fast} and θ_{slow} change. In general, when θ_{fast} is sufficiently large, the surface with fast kinetics will determine the overpotential (η) of that electrode. Conversely, as θ_{fast} approaches zero, the kinetically slow surface must supply the current. Therefore, η must increase in order to maintain a constant current. This logic can be further expanded to include contributions from more than two parallel processes on an electrode. In the general case, eq 5 can be expressed as

$$I_t = \sum_p I_p = \sum_p g_p(\eta)\theta_p k^0_p \quad (6)$$

where p is an index of the contributing processes.

The total current of a Li−Li symmetric cell will have contributions from a variety of parallel processes on both the anode and cathode. As observed in the visualization cell, the major contributing processes at the anode are electrodissolution from existing dendrites (I_{den}), planar bulk Li (I_{bulk}), and pitted surfaces (I_{pit}). At the cathode, the major contributing processes are electrodeposition onto dendrite surfaces (I_{grow}) and nucleation of new dendrites (I_{nuc}). The total current must be constant at both electrodes to guarantee continuity. Also, by definition, $\sum_p \theta_p = 1$ because the area fractions associated with each process must sum to unity. A

Scheme 2[a]

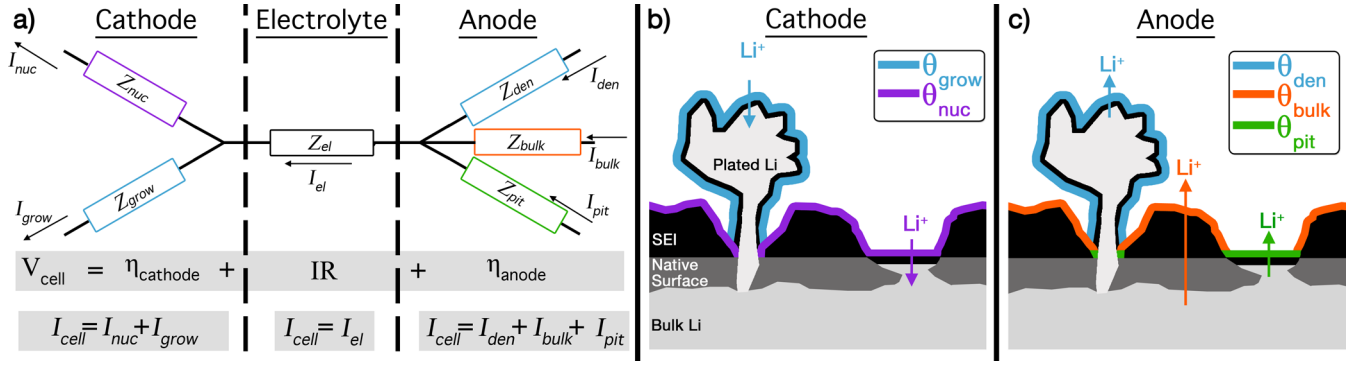

[a](a) A schematic representation of reaction pathways for the cathode, anode, and electrolyte. The overpotential at each electrode is a function of the total current, which is equal to a sum of current contributions from each reaction pathway at that electrode. The magnitude of current that passes through each pathway is dependent on the impedance associated with that pathway. The dominant pathway for current at each electrode is associated with the processes with the lowest impedance (Z_p), which has the largest influence on the electrode overpotential. A schematic representation of the regions associated with the area fraction of each process, θ_p, is shown for the cathode (b) and for the anode (c). The impedance of each process is inversely proportional to θ_p and ΔG_p, as discussed in section 4.1.

DOI: 10.1021/acscentsci.6b00260
ACS Cent. Sci. 2016, 2, 790−801

schematic circuit diagram of this behavior is shown in Scheme 2.

The differences in the kinetic constants for each of the contributing processes can be understood in terms of activation energy. Mathematically, these two quantities are related by

$$k_p^0 = A_p\, e^{-\Delta G_p/RT} \tag{7}$$

where k_p^0 is the rate constant for the process p, A_p is the corresponding Arrhenius constant, and ΔG_p is the total energy barrier for the process, which accounts for transport through the surface layer as well as charge transfer at the electrode surface. These different energy barriers arise from intrinsic differences in nature of the SEI layers associated with the respective processes (e.g. the SEI layer on the dendrites may be thinner and/or more defective than that on the bulk electrode due to continuous fracturing as the dendrite grows. Therefore, it may have an entirely different chemical composition, leading to the lower energy barrier).[36]

For a given electrode, if it is assumed that ΔG_p remains relatively constant for each process throughout cycling, then the change in the area fraction (θ_p) as morphology evolves will cause the current to shift reaction pathways (Scheme 2). The total current will be dominated by the reaction pathway with lowest net impedance, Z_p, which is inversely proportional to both θ_p and the rate constant (k_p^0) for that specific process. The total voltage for the cell, V_{cell}, is a summation of the voltage contributions in series:

$$V_{cell} = \eta_{anode} + \Delta V_{IR} + \eta_{cathode} \tag{8}$$

where ΔV_{IR} is the potential drop due to the internal resistance of the cell. Since constant current is applied in our experiment, we assume changes in ΔV_{IR} as a function of time to be negligible. We also assume that the initial cycling of the cell is negligibly affected by the relaxation behavior of concentration gradients (see Figures S3 and S9).

Under these assumptions, any changes in cell voltage for a small differential time element must be related only to changes in electrode overpotentials:

$$\delta V_{cell} = \delta\eta_{anode} + \delta\eta_{cathode} \tag{9}$$

where δV_{cell} is the differential change in cell voltage, $\delta\eta_{anode}$ is the differential change in anode overpotential, and $\delta\eta_{cathode}$ is the differential change in cathode overpotential. The electrode overpotentials described in eq 9 are directly related to the activation barrier(s) of the dominant process(es) at each electrode, as described in eq 5 through 7.

4.2. Visualization Cell Interpretation. Using the general framework presented in the previous subsection, we can directly attribute δV_{cell} to the dominant processes occurring on each electrode at specific points in a half-cycle. Through use of three-electrode measurements, shown in Figure 3, the contributions from individual electrodes can be directly observed. This allows for a detailed interpretation of voltage traces through analysis of the coupled morphological and electrochemical behavior of Li metal electrodes.

4.2.1. The First Half-Cycle. A schematic representation of the visualization cell observations described in section 2.2 is shown in Figure 4. The initial pristine Li surfaces are composed of a bulk metallic Li electrode, a native surface layer (formed during manufacturing and storage, which may contain several species including, nitrides, LiOH, Li_2O, and Li_2CO_3),[37] and an SEI that forms upon exposure to the electrolyte (Figure 4a). During the

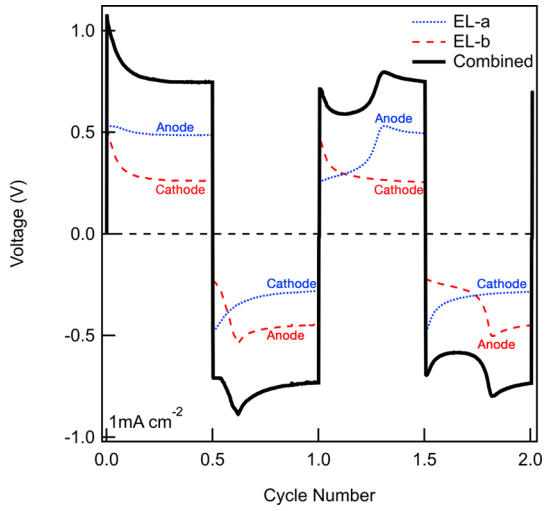

Figure 3. Three-electrode measurements showing the cell polarization contributions from each electrode. Here EL-b is the working electrode (WE) and EL-a is the counter electrode (CE). For visual aid, CE has been multiplied by −1 such that the total cell polarization = CE + WE. Voltage is vs Li/Li^+.

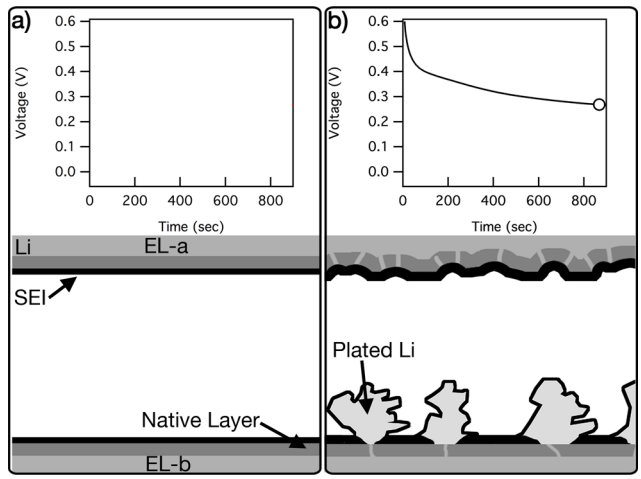

Figure 4. Schematic representation of experimental observations in section 2.2. The upper electrode is EL-a, and the lower electrode is EL-b. (a) Before cycling. (b) End of first half-cycle: pits form at EL-a (anode), and dendrites grow on EL-b (cathode).

first half-cycle (Figure 4b), the only process occurring at the anode (EL-a, the top electrode in Figure 4) is pitting because no previously formed dendrites exist. On the cathode (EL-b, the bottom electrode in Figure 4), the observations from the visualization cell indicate that Li does not plate uniformly on the electrode surface, but rather through the nucleation ("nuc") and growth ("grow") of dendrites. Nucleation inherently involves an additional energy barrier, and thus the kinetics of growth is significantly faster than that of nucleation ($k_{nuc}^0 < k_{grow}^0$).

As dendrites nucleate, the dominant reaction pathway at the cathode transitions from nucleation to growth (Scheme 2). This is consistent with the visualization cell observation that additional Li^+ preferentially deposits on the dendrite surfaces, rather than forming new nucleation sites (Figure 1b; Figure 4b; Video 1). As the area fraction of the growing dendrites (θ_{grow}) increases, the impedance associated with dendrite growth (Z_{grow}) decreases throughout the half-cycle, such that $I_{grow} > I_{nuc}$

DOI: 10.1021/acscentsci.6b00260
ACS Cent. Sci. 2016, 2, 790−801

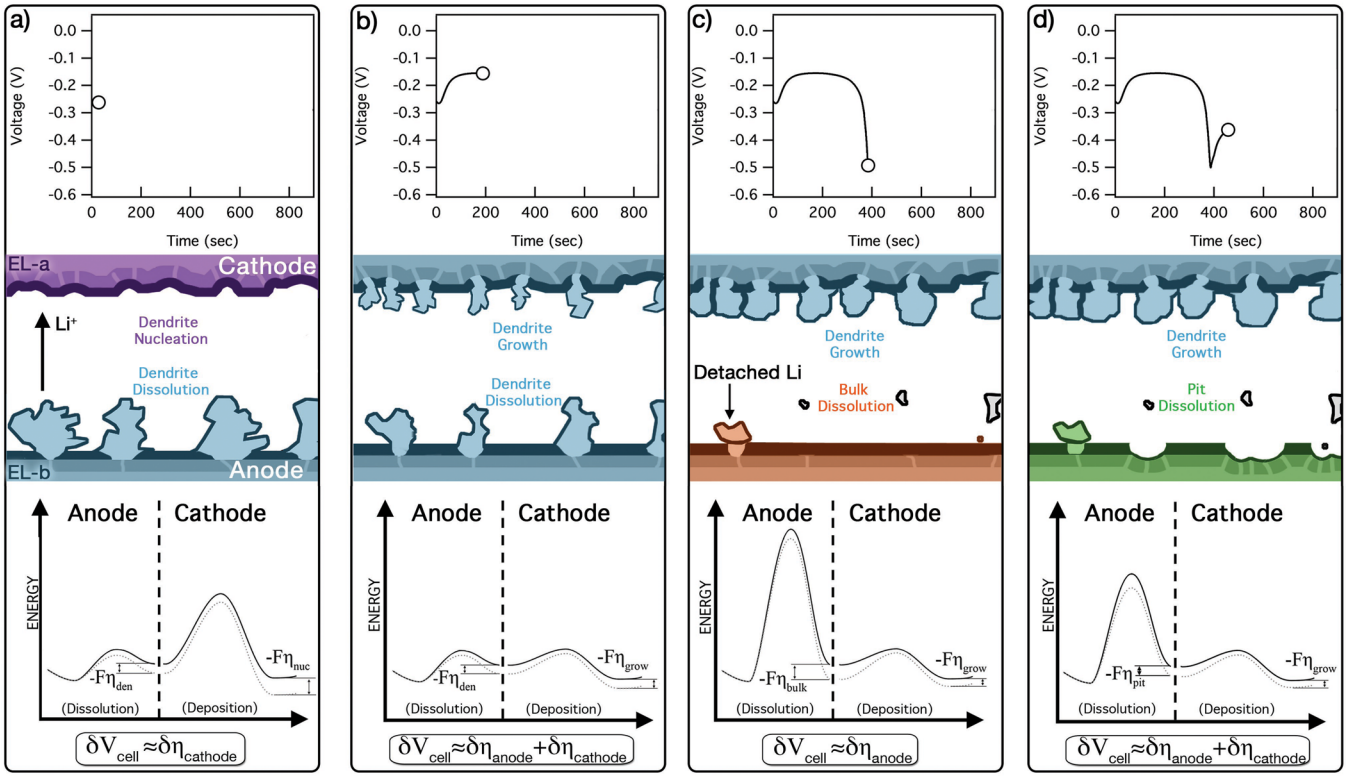

Figure 5. Changes in cell polarization (top) are correlated with a schematic representation of morphology (middle; color-coded to match the appropriate reaction pathway as described in Scheme 2) and energy barrier diagrams (bottom). In the energy barrier diagram the difference between the solid and dashed lines is for the equilibrium and bias conditions, respectively. The energy barrier diagrams display dominant reaction pathways at each electrode. This is shown at four points in the voltage trace: (a) Beginning of half-cycle: dendrite nucleation is the kinetically slow process. (b) Cell polarization minimum: dendrites present on both electrodes, kinetically fast reaction pathways. (c) Cell polarization maximum: "active" Li removed from dendrites; electrodissolution transitions to kinetically slow bulk dissolution. (d) Second decrease in cell polarization: pitting becomes the kinetically slow process.

(Scheme 2). Similarly, electrodissolution at the anode transitions from Li^+ removal from the bulk surface to preferential dissolution from pits ("pit"). This interpretation is confirmed by the three-electrode measurements. As can be seen in Figure 3, the initial drop in cell polarization during the first half-cycle is predominantly due to the drop in overpotential at the cathode, EL-b, which can be explained by the transition from dendrite nucleation to dendrite growth and the subsequent increase in surface area of the dendrites. The effect of pitting on the anode is noticeable, but lower in magnitude than the cathode effects.

4.2.2. The Second Half-Cycle. The characteristic "peaking" behavior previously discussed is observed in the voltage profile for subsequent half-cycles (Figure 1). In the second half-cycle (Figure 4b), EL-b becomes the anode and EL-a becomes the cathode (Figure 5a). At this point, the area fraction of dendrites on the surface of El-b, which was equal to θ_{grow} in the previous half-cycle, is now equal to θ_{den}. As dendritic and bulk Li now exist on the anode, the proportion of current flowing though each reaction pathway will be determined by the impedance of each pathway. This impedance is a function of the energy barrier, ΔG_p, associated with each process (eq 7). Schematic energy barrier diagrams are shown in the lower panels of Figure 5, which correlates kinetics to the morphology changes shown in the middle panel (further details in the Supporting Information).

Immediately upon switching polarity (Figure 5a; Video 1 0:10), Li electrodissolution occurs preferentially from the dendrites on EL-b because $\Delta G_{den}^{anode} < \Delta G_{bulk}^{anode}$, and thus $k_{den}^0 > k_{bulk}^0$. Simultaneously, a maximum in cell voltage is observed, which is due to the large activation barrier associated with nucleation ($\Delta G_{nuc}^{cathode}$) on EL-a (Figure S10). At this point, the kinetics of each electrode are dominated by nucleation at the cathode and electrodissolution from dendrites at the anode. These results are also in agreement with the numerical model, where θ_{fast} is large on the anode and small on the cathode. As shown in Figure 5a, the largest contribution to δV_{cell} is associated with the activation barrier to nucleation on the cathode ($\Delta G_{nuc}^{cathode} > \Delta G_{den}^{anode}$). This can be clearly observed in the three-electrode measurements of Figure 3 as the initial peak is always associated with the cathode.

As deposition continues onto EL-a, cell polarization decreases. The steep initial decrease in polarization corresponds to a transition in reaction pathways from nucleation to growth of dendrites on EL-a. This occurs because θ_{grow} increases and $k_{grow}^0 > k_{nuc}^0$ ($\Delta G_{grow}^{cathode} < \Delta G_{nuc}^{cathode}$). After the transition has occurred, a local minimum in cell voltage is observed (Figure 5b; Video 1 0:11). At this point, the dominant process at the cathode is growth of dendrites and at the anode is dissolution from dendrites. The kinetics of both of these processes are relatively fast, resulting in a minimum of V_{cell} (Figure 5b). This minimum is also observed in the numerical model (section 3, Figure 2), when θ_{fast} is relatively large on both electrodes.

As active Li in the form of dendrites on EL-b is depleted, θ_{den} decreases, leading to an increase in cell voltage. Once θ_{den} is sufficiently small, it becomes necessary to dissolve Li from the

DOI: 10.1021/acscentsci.6b00260
ACS Cent. Sci. 2016, 2, 790−801

surrounding bulk surface in addition to the dendrites. This causes a transition between reaction pathways on EL-b. As θ_{den} approaches zero, a maximum in cell voltage occurs (Figure 5c; Video 1 0:14). At this point in the process, Li electrodissolution from the bulk surface, a kinetically slow process (associated with k^0_{bulk} and ΔG^{anode}_{bulk}), dominates on EL-b. This is also observed in the three-electrode measurements and the numerical model, as θ_{fast} on El-b becomes zero. Since the cathode is undergoing dendrite growth at this point, which is a kinetically faster process, the largest contribution to δV_{cell} is associated with the activation barrier to electrodissolution from the anode ($\Delta G^{anode}_{bulk} > \Delta G^{cathode}_{grow}$), as shown in Figure 5c. Again this can be distinctly seen in Figure 3 as the second peak is always associated with the anode.

As electrodissolution continues from EL-b, a second decrease in cell polarization is observed. This corresponds to a transition in reaction pathways, resulting in preferential electrodissolution from pits on EL-b, rather than the bulk surface (Figure 5d; Video 1 0:19). The transition is driven by an increase in θ_{pit} and the fact that $k^0_{pit} > k^0_{bulk}$ because $\Delta G^{anode}_{pit} < \Delta G^{anode}_{bulk}$. At this point, the dominant process at the cathode is growth of dendrites and at the anode is dissolution from pits. As θ_{pit} and θ_{grow} continue to increase, V_{cell} continues to decrease (Figure 5d). We note that this behavior is only partially captured by the numerical model because the model accounts for the increase in θ_{fast} on El-a from dendrite growth but does not explicitly account for pitting. Nevertheless, the agreement between the two- and three-electrode experimental data and simulated voltage traces indicates that the general behavior of the voltage originates from the transitions between kinetically fast and slow processes.

4.2.3. Summary of Voltage Trace Interpretation. To provide a visual aid for the discussion above, Figure 6 summarizes the dominant reaction pathways at each electrode as a function of time during the half-cycle for a two-electrode measurement. This clearly shows the three different reaction pathways associated with electrodissolution and the two related to electrodeposition, as described previously in Scheme 2. This understanding allows for detailed information to be extracted about Li metal electrodes, simply by analyzing the voltage traces from galvanostatic cycling. Furthermore, Figure S11 shows that this behavior is observed at 0.5, 0.75, 1, 2, 5, and 10 mA/cm^2, making the interpretation of these voltage traces applicable for conditions of practical battery operation.

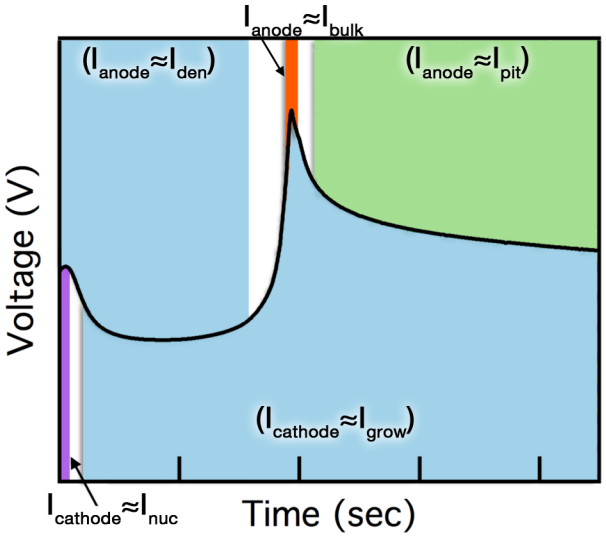

Figure 6. An experimental two-electrode voltage trace showing the dominant reaction pathways at each electrode as a function of time. Shaded regions indicate dominant pathways at the anode (above profile) and cathode (below profile). Unshaded areas represent regions of transition between pathways.

4.3. Effect of Electrolyte on Electrode Performance and Voltage Profiles. To demonstrate how the understanding of section 4.2 can be more generally applied, we intentionally selected three electrolytes (1 M $LiPF_6$ EC:DMC (1:1); 4 M LiFSI DME; and 1 M LiTFSI DOL:DME (1:1) with 0.18 M Li_2S_8 and 2 wt % $LiNO_3$) with significantly different additives, concentrations, solvents, and salts (see the Supporting Information for more details). The general optimization of these electrolytes in Li−Cu cells has been well documented elsewhere.[11,22] By utilizing Li−Li symmetric cells and intentionally selecting these three significantly different electrolyte systems with known performance differences, we demonstrate that interpretation of voltage traces is a robust method for gaining mechanistic insight into Li metal electrode behavior. For simplicity we will refer to each system only by its salt (i.e., $LiPF_6$, LiFSI, LiTFSI), however the compositions remain identical to those listed above. Specifically the LIFSI and LiTFSI are being investigated as potential electrolytes for Li−S batteries, making them of significant interest to the research community.

4.3.1. Visualization Cell Results for a Variety of Electrolyte Compositions. The visualization cell results for the LiFSI and LiTFSI electrolyte systems are shown in Video 2 and Video 3 respectively. These videos, in addition to Figure 7a, show that the ether-based electrolytes clearly increase nucleation density, reduce dendrite size, and lead to more complete surface coverage, especially for the LiTFSI electrolyte. As seen in the videos, the same general form of the voltage trace is observed for the LiFSI and LiTSFI systems (further details in Figure S13). However, after a few cycles, the abruptness of the transitions (δV_{cell}) becomes significantly less pronounced than for the $LiPF_6$ system. This is consistent with observations in the numerical model that, as the difference between k^0_{fast} and k^0_{slow} becomes small, the transitions become less well-defined (Supporting Information, section S7). Additionally, the voltage maximum associated with transitioning between reaction pathways on the anode surface occurs later in the half-cycle (i.e., the amount of time between the voltage minimum and maximum becomes larger). We note that, in the ether-based electrolytes, the time required to observe this polarization maximum may be longer than the duration of the previous half-cycle (Figure 7c). For this reason, the voltage traces observed during periodic galvanostatic cycling terminate before the final decrease in cell polarization occurs (Figure S13). This correlates to a greater duration of simultaneous Li electrodissolution from the bulk and dendrites as the reaction pathway transitions, as discussed in section 4.2.2. Visually this can be clearly observed in both videos (Video 2 0:34−0:37; Video 3 0:34−0:38).

In order to better understand these effects, time-dependent EIS measurements were performed to study the formation, growth, and impedance of the SEI on fresh Li surfaces (Figure S14). The data show that the ether-based electrolytes form lower impedance and more stable SEI layers compared to the $LiPF_6$ system. These SEI layers thus have a lower energy barrier for electrodissolution at the anode surface, which leads to closer values of the effective rate constants. As a result, the transition in reaction pathways begins sooner in the half-cycle and lasts

DOI: 10.1021/acscentsci.6b00260
ACS Cent. Sci. 2016, 2, 790−801

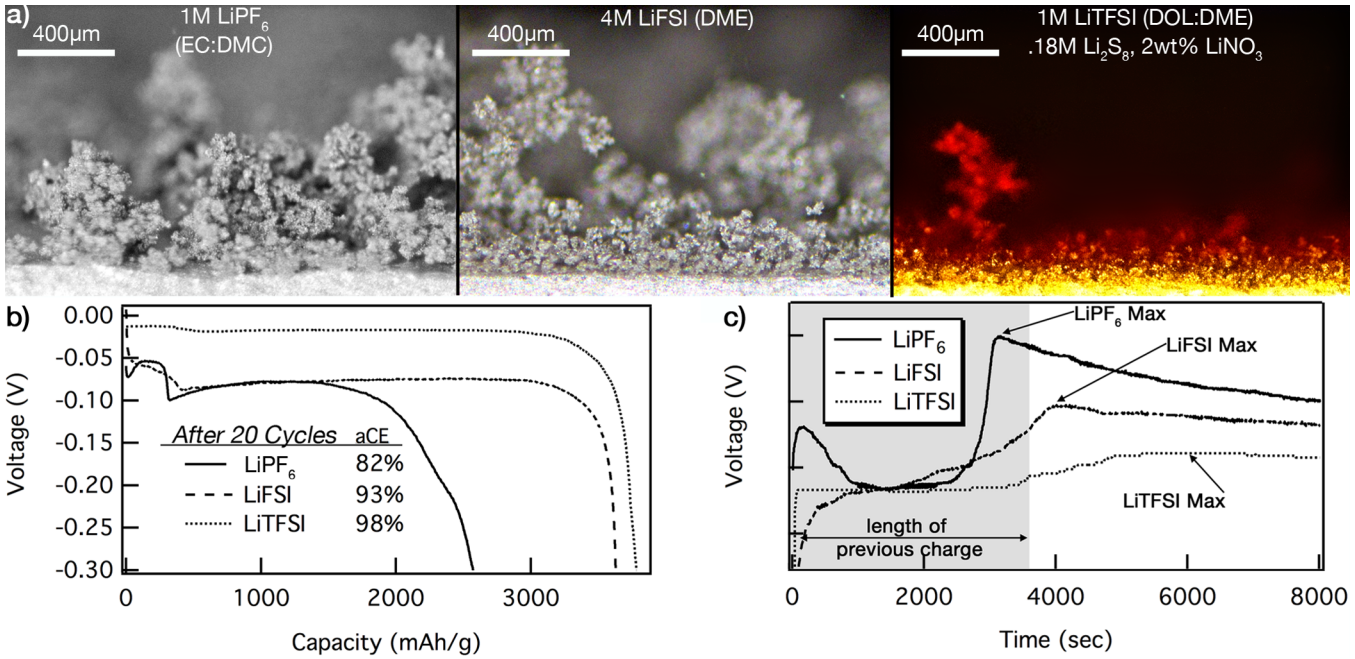

Figure 7. Comparison of three very different electrolyte systems ($LiPF_6$, LiFSI, and LiTFSI). (a) Visualization cell images after 900 s of deposition at 5 mA cm^{-2}. A clear difference in dendrite size, nucleation density, and surface coverage is observed. (b) Cell discharge curves at 1 mA cm^{-2} showing remaining capacity after 20 cycles (theoretical capacity 3860 mAh g^{-1}). This performance can be linked to peak position in panel c, where voltage traces for each electrolyte system are shown.

for a longer duration. In other words, the unshaded regions of Figure 6 (which for $LiPF_6$ are well-defined and relatively narrow) become wider.

4.3.2. Comparing Voltage Traces with Performance in Coin Cells Using Different Electrolyte Compositions. To show how the understanding of section 4.3.1 can be observed in coin cells, Li−Li symmetric cells were fabricated using each electrolyte system and Li−Cu laminate electrodes (Rockwood Li, 50 μm of Li on 10 μm of Cu). The cells were cycled 20 times at 1 mA cm^{-2}, such that a planar equivalent of 4.8 μm of Li was transferred during each half-cycle (1C rate). After cycling, Li on one electrode was completely dissolved from the Cu to determine the amount of Li lost during cycling. By calculating the average amount of Li lost during each cycle, an average Coulombic efficiency (aCE) for the Li electrode can be obtained (further details in Figure S15). This is a modified version of a method developed by Aurbach et al.[38]

In Figure 7b,c aCE is compared to the position of the voltage maximum associated with transitioning between reaction pathways on the anode surface. Figure 7b shows significantly less capacity loss for the ether-based electrolytes compared to the carbonate based $LiPF_6$. This corresponds to aCE values of 82% ($LiPF_6$), 93% (LiFSI), and 98% (LiTFSI). A detailed view of the voltage profile for an extended half-cycle is shown for each system in Figure 7c. Consistent with section 4.2, the $LiPF_6$ cell exhibited distinct transitions between reaction pathways. By comparison, the LiFSI coin cell exhibited a more blunted cell polarization maximum that occurs at a later time than the peak in $LiPF_6$, indicating less distinct transitions between reaction pathways and a lower voltage hysteresis. Finally, the LiTFSI cell displayed the lowest overpotential, the latest, most blunted cell polarization maximum, and the lowest voltage hysteresis. The shifting of these cell polarization maximums is directly correlated with an increase in the aCE value. Comparing Figures 7a and 7c also shows that a smaller magnitude and delayed cell polarization maximum is directly related to denser/smaller dendrites that completely cover the surface. Since this voltage behavior is observed in a wide range of battery architectures, this interpretation allows for a cycle-by-cycle comparison of Li metal electrode performance. Understanding the dominant reaction pathways at specific points in time provides a "window" into the time-dependent morphological and electrochemical changes occurring within coin cells, where we are typically "blind" to morphology.

5. EXPERIMENTAL DETAILS

All air sensitive materials were handled in an argon filled glovebox (MBraun), with water and moisture levels below 1 ppm. The $LiPF_6$ electrolyte (Soulbrain) contained <7 ppm water, while the battery-grade solvents used in the sulfur-based electrolytes were purchased from BASF Inc. and contained <20 ppm water.

5.1. Visualization Cell Tests. Operando tests were conducted in a custom-built visualization cell (Figure S1), allowing simultaneous collection of electrochemical and morphological information. The entire assembly is air-tight with a quartz viewing window and O-ring seal so that it can be removed from the glovebox after assembly and placed under an optical microscope for viewing. Air-tight electrical feedthroughs connect the electrodes with the potentiostat. All visualization cell experiments were carried out using a Gamry 1000 or Biologic VSP potentiostat using 1 M $LiPF_6$ in 1:1 ethylene carbonate/dimethylcarbonate (EC/DMC), 1 M LiTFSI in 1,3-dioxolane/1,2-dimethoxyethane (DOL:DME) with 0.18 M Li_2S_8 and 2 wt % $LiNO_3$, and 4 M LiFSI in DME. The LiFSI and LiTFSI electrolytes were synthesized following a formulation similar to those described previously.[11,22] For each half-cycle, 4.5 C cm^{-2} of charge was passed for 10 complete charge and discharge cycles. After each half-cycle, the system was allowed to relax for 30 s. The optical microscopy

DOI: 10.1021/acscentsci.6b00260
ACS Cent. Sci. 2016, 2, 790−801

images were taken with a Nikon LV150N microscope at 5× with a plan objective, n.a. 0.10, w.d. 31 mm. A total of 90 images were taken per half-cycle in order to create the video micrographs. The videos are 100× playback speed.

5.2. Three-Electrode Measurements. Three-electrode measurements were experimentally conducted using a hermetically sealed glassware setup. The reference electrode (RE) was a scraped, cleaned, and stabilized piece of Li foil. The data was collected using the bipotentiostat capabilities of the Biologic VSP system, which can measure the potential of the counter electrode and working electrode vs RE simultaneously.

5.3. Coin Cell Tests. Symmetric Li coin cells were assembled with CR2032 coin cell shells, spacers, and wave springs (MTI Corp.). The Li−Cu laminate electrodes (99.9%, Rockwood Lithium) were pentane cleaned[12] and immediately assembled into coin cells using 45 μL of the electrolytes described above. A hydraulic crimping press was used to compress these coin cells to 1000 psi. Cell cycling was completed on a Landt 2001a battery testing system.

6. CONCLUSIONS

In this work, we have shown through operando video evidence and numerical modeling that galvanostatic voltage traces can be directly correlated to changes in morphology of Li metal electrodes in Li−Li symmetric cells. This correlation has led to several key points of understanding:

6.1. The Evolution of Dendrite Morphology Is Driven by Transitions between Reaction Pathways. During the initial half-cycle, inhomogeneous dendrite nucleation occurs at the cathode. Since the SEI on freshly plated Li will have faster reaction kinetics than the bulk surface, subsequent Li deposition will preferentially occur on existing dendrites rather than nucleating new dendrites. The degree to which dendrite growth is more favorable than nucleation is dictated by the SEI, which depends on the electrolyte system. Upon switching polarity, the dominant reaction pathway at the anode is kinetically fast dissolution of dendritic Li. As the amount of active Li within the dendrites approaches zero, a characteristic increase in cell polarization appears, due to a transition to kinetically slower dissolution from the bulk surface.

6.2. Pitting Occurs Once Dissolution from the Bulk Surface Begins. Electrodissolution from the bulk leads to the formation of pits. Subsequently, as the surface layers are fractured during pitting, kinetically faster reaction pathways are formed. As dissolution continues, the surface area associated with pits continues to increase, resulting in decreasing cell polarization. Upon changing polarity Li dendrites preferentially nucleate within these pits.

6.3. Transitions between Reaction Pathways Dictate Changes in Voltage. After the first half-cycle, the initial portion of the voltage trace is dominated by the cathode, as a transition occurs from dendrite nucleation to growth. After the minimum cell polarization is reached, the kinetics at the anode begin to dominate the voltage trace, as the surface area of the kinetically fast dendrites decreases. This leads to a transition in reaction pathway from dissolution of dendrites to dissolution from the bulk surface, causing a cell polarization maximum. As pitting occurs, the decrease in cell polarization is driven by increasing surface area of both pits at the anode and dendrites at the cathode.

6.4. Voltage Traces Can Be Correlated to Electrode Performance. Variations in the voltage trace shape in different electrolyte systems can be linked to cell performance. For systems with poorer performance, the peak associated with the transition between dominant reaction pathways at the anode has a steeper slope, occurs at an earlier time in the half-cycle, and demonstrates higher voltage hysteresis. Conversely, for systems with superior performance, that maximum is less distinct, occurs at a later time, and has a smaller magnitude. In general, a shifting of the cell polarization maximum can be directly correlated to improved CE.

6.5. Future Impact. These results provide significant new insight into the behavior of Li metal electrodes, which can assist researchers in the quest to achieve commercially viable Li metal anode secondary batteries. Specifically, from the fundamental understanding presented in this work, it can be determined that in order to improve performance, safety, and lifetime of Li metal anodes, the non-uniform reactivity of the surface must be homogenized. Spatial variations in reaction kinetics drive the morphological evolution of the electrode, which can be directly related to the shape of voltage traces in Li symmetric cells. Through this study we have demonstrated that, by minimizing spatial variations in local surface reactivity (i.e., making the reaction constants k_{fast} and k_{slow} as similar as possible), dendrites will be more evenly distributed, smaller, and more reversible. This homogenization of the local reaction constants along the electrode surface can be accomplished in a myriad of ways, including the design of electrolytes that form more homogeneous and stable SEI layers, or by modification of the electrode surface reactivity through protective coatings that promote spatial homogeneity of Li ion flux across the dynamic electrode−electrolyte interface. Furthermore, the results and experiments described in this work can be applied to a range of battery chemistries, including Li ion, Li−S, Li−air, Zn−air, Na ion, and more.

■ ASSOCIATED CONTENT

Supporting Information

The Supporting Information is available free of charge on the ACS Publications website at DOI: 10.1021/acscentsci.6b00260.

Introductory lecture (MOV)
Additional text and figures (PDF)
Synchronized morphology and voltage changes for 1 M $LiPF_6$ EC/DMC cycled at 5 mA/cm^2 (MOV)
Synchronized morphology and voltage changes for 4 M LiFSI DME cycled at 5 mA/cm^2 (MOV)
Synchronized morphology and voltage changes for 1 M LiTFSI DOL/DME 0.18 M Li_2S_8 and 2 wt % $LiNO_3$ cycled at 5 mA/cm^2 (MOV)
Synchronized morphology and voltage changes for 1 M $LiPF_6$ EC/DMC with separator for extended periods of cycling at 1 mA/cm^2 (MOV)

■ AUTHOR INFORMATION

Corresponding Author

*E-mail: ndasgupt@umich.edu.

Notes

The authors declare no competing financial interest.

■ ACKNOWLEDGMENTS

This work was supported by the Joint Center for Energy Storage Research (JCESR), an Energy Innovation Hub funded by the U.S. Department of Energy, Office of Science, Basic Energy Sciences, Grant No. DE-AC02-06CH11357. E.K. acknowledges that this material is based upon work supported

DOI: 10.1021/acscentsci.6b00260
ACS Cent. Sci. 2016, 2, 790−801

by the National Science Foundation Graduate Research Fellowship under Grant No. (DGE 1256260).

■ ABBREVIATIONS

EV, electric vehicle; LiBs, lithium ion batteries; CE, Coulombic efficiency; SEI, solid electrolyte interphase; TEM, transmission electron microscopy; ALD, atomic layer deposition; EIS, electrochemical impedance spectroscopy; SEM, scanning electron microscopy; $LiPF_6$, lithium hexafluorophosphate; EC, ethylene carbonate; DMC, dimethylcarbonate; EL-a, electrode *not* visible during visualization cell cycling; EL-b, electrode visible during visualization cell cycling; PNP, Poisson−Nernst−Planck; FDM, finite difference method; LiFSI, lithium bis-(fluorosulfonyl)imide; DME, 1,2-dimethoxyethane; DOL, 1,3-dioxolane; LiTFSI, lithium bistrifluoromethanesulfonimidate; aCE, average Coulombic efficiency

■ REFERENCES

(1) Bruce, P. G.; Hardwick, L. J.; Abraham, K. M. Lithium-Air and Lithium-Sulfur Batteries. *MRS Bull.* **2011**, *36*, 506−512.
(2) Gallagher, K. G.; Goebel, S.; Greszler, T.; Mathias, M.; Oelerich, W.; Eroglu, D.; Srinivasan, V. Quantifying the Promise of Lithium−air Batteries for Electric Vehicles. *Energy Environ. Sci.* **2014**, *7*, 1555−1563.
(3) Bieker, G.; Bieker, P. M.; Winter, M. Electrochemical In Situ Investigations of the SEI and Dendrite Formation on the Lithium Metal Anode. *Phys. Chem. Chem. Phys.* **2015**, *17*, 8670−8679.
(4) Aurbach, D. Review of Selected Electrode-Solution Interactions Which Determine the Performance of Li and Li Ion Batteries. *J. Power Sources* **2000**, *89*, 206−218.
(5) Harry, K. J.; Hallinan, D. T.; Parkinson, D. Y.; MacDowell, A. a; Balsara, N. P. Detection of Subsurface Structures underneath Dendrites Formed on Cycled Lithium Metal Electrodes. *Nat. Mater.* **2014**, *13*, 69−73.
(6) Yoshimatsu, I.; Hirai, T.; Yamaki, J. Lithium Electrode Morphology during Cycling in Lithium Cells. *J. Electrochem. Soc.* **1988**, *135*, 2422−2427.
(7) Selim, R.; Bro, P. Some Observations on Rechargeable Lithium Electrodes in a Propylene Carbonate Electrolyte. *J. Electrochem. Soc.* **1974**, *121*, 1457−1459.
(8) Ding, F.; Xu, W.; Graff, G. L.; Zhang, J.; Sushko, M. L.; Chen, X.; Shao, Y.; Engelhard, M. H.; Nie, Z.; Xiao, J.; et al. Dendrite-Free Lithium Deposition via Self-Healing Electrostatic Shield Mechanism. *J. Am. Chem. Soc.* **2013**, *135*, 4450−4456.
(9) Schweikert, N.; Hofmann, A.; Schulz, M.; Scheuermann, M.; Boles, S. T.; Hanemann, T.; Hahn, H.; Indris, S. Suppressed Lithium Dendrite Growth in Lithium Batteries Using Ionic Liquid Electrolytes: Investigation by Electrochemical Impedance Spectroscopy, Scanning Electron Microscopy, and in Situ 7 Li Nuclear Magnetic Resonance Spectroscopy. *J. Power Sources* **2013**, *228*, 237−243.
(10) Xu, W.; Wang, J.; Ding, F.; Chen, X.; Nasybulin, E.; Zhang, Y.; Zhang, J.-G. Lithium Metal Anodes for Rechargeable Batteries. *Energy Environ. Sci.* **2014**, *7*, 513−537.
(11) Qian, J.; Henderson, W. a.; Xu, W.; Bhattacharya, P.; Engelhard, M.; Borodin, O.; Zhang, J.-G. High Rate and Stable Cycling of Lithium Metal Anode. *Nat. Commun.* **2015**, *6*, 6362−6371.
(12) Kazyak, E.; Wood, K. N.; Dasgupta, N. P. Improved Cycle Life and Stability of Lithium Metal Anodes through Ultrathin Atomic Layer Deposition Surface Treatments. *Chem. Mater.* **2015**, *27*, 6457−6462.
(13) Mehdi, B. L.; Qian, J.; Nasybulin, E.; Park, C.; Welch, D. a.; Faller, R.; Mehta, H.; Henderson, W. a.; Xu, W.; Wang, C. M.; et al. Observation and Quantification of Nanoscale Processes in Lithium Batteries by Operando Electrochemical (S)TEM. *Nano Lett.* **2015**, *15*, 2168−2173.
(14) López, C. M.; Vaughey, J. T.; Dees, D. W. Morphological Transitions on Lithium Metal Anodes. *J. Electrochem. Soc.* **2009**, *156*, A726−A729.
(15) Brandt, K. Historical Development of Secondary Lithium Batteries. *Solid State Ionics* **1994**, *69*, 173−183.
(16) Lin, D.; Liu, Y.; Liang, Z.; Lee, H.-W.; Sun, J.; Wang, H.; Yan, K.; Xie, J.; Cui, Y. Layered Reduced Graphene Oxide with Nanoscale Interlayer Gaps as a Stable Host for Lithium Metal Anodes. *Nat. Nanotechnol.* **2016**, *11*, 626−632.
(17) Liang, Z.; Lin, D.; Zhao, J.; Lu, Z.; Liu, Y.; Liu, C.; Lu, Y.; Wang, H.; Yan, K.; Tao, X.; et al. Composite Lithium Metal Anode by Melt Infusion of Lithium into a 3D Conducting Scaffold with Lithiophilic Coating. *Proc. Natl. Acad. Sci. U. S. A.* **2016**, *113*, 2862−2867.
(18) Basile, A.; Bhatt, A. I.; O'Mullane, A. P. Stabilizing Lithium Metal Using Ionic Liquids for Long-Lived Batteries. *Nat. Commun.* **2016**, *7*, 1−11.
(19) Park, M. S.; Ma, S. B.; Lee, D. J.; Im, D.; Doo, S.-G.; Yamamoto, O. A Highly Reversible Lithium Metal Anode. *Sci. Rep.* **2014**, *4*, 3815−3823.
(20) Love, C. T.; Baturina, O. a.; Swider-Lyons, K. E. Observation of Lithium Dendrites at Ambient Temperature and Below. *ECS Electrochem. Lett.* **2015**, *4*, A24−A27.
(21) Rosso, M.; Brissot, C.; Teyssot, A.; Dollé, M.; Sannier, L.; Tarascon, J.-M.; Bouchet, R.; Lascaud, S. Dendrite Short-Circuit and Fuse Effect on Li/polymer/Li Cells. *Electrochim. Acta* **2006**, *51*, 5334−5340.
(22) Li, W.; Yao, H.; Yan, K.; Zheng, G.; Liang, Z.; Chiang, Y.-M.; Cui, Y. The Synergetic Effect of Lithium Polysulfide and Lithium Nitrate to Prevent Lithium Dendrite Growth. *Nat. Commun.* **2015**, *6*, 7436−7444.
(23) Wu, H.; Zhuo, D.; Kong, D.; Cui, Y. Improving Battery Safety by Early Detection of Internal Shorting with a Bifunctional Separator. *Nat. Commun.* **2014**, *5*, 5193−5199.
(24) Stark, J. K.; Ding, Y.; Kohl, P. A. Nucleation of Electrodeposited Lithium Metal: Dendritic Growth and the Effect of Co-Deposited Sodium. *J. Electrochem. Soc.* **2013**, *160*, D337−D342.
(25) Zheng, G.; Lee, S. W.; Liang, Z.; Lee, H.-W.; Yan, K.; Yao, H.; Wang, H.; Li, W.; Chu, S.; Cui, Y. Interconnected Hollow Carbon Nanospheres for Stable Lithium Metal Anodes. *Nat. Nanotechnol.* **2014**, *9*, 618−623.
(26) Aurbach, D. The Correlation Between Surface Chemistry, Surface Morphology, and Cycling Efficiency of Lithium Electrodes in a Few Polar Aprotic Systems. *J. Electrochem. Soc.* **1989**, *136*, 3198−3205.
(27) Kozen, A. C.; Lin, C.-F.; Pearse, A. J.; Schroeder, M. A.; Han, X.; Hu, L.; Lee, S.-B.; Rubloff, G. W.; Noked, M. Next-Generation Lithium Metal Anode Engineering via Atomic Layer Deposition. *ACS Nano* **2015**, *9*, 5884−5892.
(28) Chadwick, A. F.; Vardar, G.; DeWitt, S.; Sleightholme, A. E. S.; Monroe, C. W.; Siegel, D. J.; Thornton, K. Computational Model of Magnesium Deposition and Dissolution for Property Determination via Cyclic Voltammetry. *J. Electrochem. Soc.* **2016**, *163*, A1813−A1821.
(29) Newman, J. S.; Thomas-Alyea, K. E. *Electrochemical Systems*; J. Wiley: Hoboken, NJ, 2004.
(30) Bard, A. J.; Faulkner, L. R. *Electrochemical Methods: Fundamentals and Applications*; John Wiley & Sons: New York, 2001.
(31) Dickinson, E. J. F.; Limon-Petersen, J. G.; Rees, N. V.; Compton, R. G. How Much Supporting Electrolyte Is Required to Make a Cyclic Voltammetry Experiment Quantitatively "Diffusional"? A Theoretical and Experimental Investigation. *J. Phys. Chem. C* **2009**, *113*, 11157−11171.
(32) Sandifer, J. R.; Buck, R. P. An Algorithm for Simulation of Transient and Alternating Current Electrical Properties of Conducting Membranes, Junctions, and One-Dimensional, Finite Galvanic Cells. *J. Phys. Chem.* **1975**, *79*, 384−392.
(33) Streeter, I.; Compton, R. G. Numerical Simulation of Potential Step Chronoamperometry at Low Concentrations of Supporting Electrolyte. *J. Phys. Chem. C* **2008**, *112*, 13716−13728.
(34) Brumleve, T. R.; Buck, R. P. Numerical Solution of the Nernst-Planck and Poisson Equation System with Applications to Membrane Electrochemistry and Solid State Physics. *J. Electroanal. Chem. Interfacial Electrochem.* **1978**, *90*, 1−31.

DOI: 10.1021/acscentsci.6b00260
ACS Cent. Sci. 2016, 2, 790−801

(35) Cohen, H.; Cooley, J. W. The Numerical Solution of the Time-Dependent Nernst-Planck Equations. *Biophys. J.* **1965**, *5*, 145−162.
(36) Huggins, R. *Advanced Batteries*; Springer US: Boston, MA, 2009.
(37) Kanamura, K.; Tamura, H.; Takehara, Z. XPS Analysis of a Lithium Surface Immersed in Propylene Carbonate Solution Containing Various Salts. *J. Electroanal. Chem.* **1992**, *333*, 127−142.
(38) Aurbach, D. Identification of Surface Films Formed on Lithium in Propylene Carbonate Solutions. *J. Electrochem. Soc.* **1987**, *134*, 1611−1620.

DOI: 10.1021/acscentsci.6b00260
ACS Cent. Sci. 2016, 2, 790−801